# One-4-All: Neural Potential Fields for Embodied Navigation

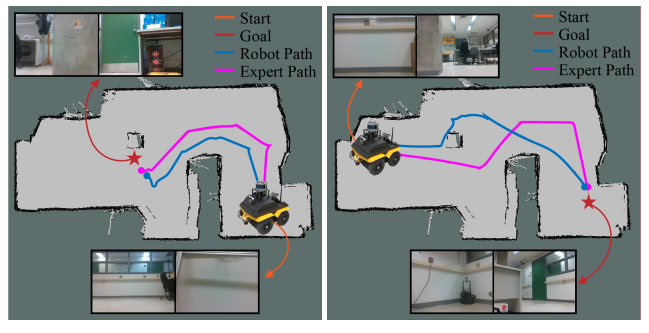
Sacha Morin\*1, Miguel Saavedra-Ruiz\*1 and Liam Paull1

Abstract—A fundamental task in robotics is to navigate between two locations. In particular, real-world navigation can require long-horizon planning using high-dimensional RGB images, which poses a substantial challenge for end-to-end learning-based approaches. Current semi-parametric methods instead achieve long-horizon navigation by combining learned modules with a topological memory of the environment, often represented as a graph over previously collected images. However, using these graphs in practice typically involves tuning a number of pruning heuristics to avoid spurious edges, limit runtime memory usage and allow reasonably fast graph queries. In this work, we present One-4-All (O4A), a method leveraging self-supervised and manifold learning to obtain a graph-free. end-to-end navigation pipeline in which the goal is specified as an image. Navigation is achieved by greedily minimizing a potential function defined continuously over the O4A latent space. Our system is trained offline on non-expert exploration sequences of RGB data and controls, and does not require any depth or pose measurements. We show that O4A can reach long-range goals in 8 simulated Gibson indoor environments, and further demonstrate successful real-world navigation using a Jackal UGV platform.a

## I. INTRODUCTION

Navigation is a crucial component in any robotics stack that requires a robot to move from one location to another. This problem is characterized by a robot's ability to identify the most efficient and feasible path between a start pose and a goal pose in a given environment. The standard approach involves first piloting the robot within the environment to build a metric map, often using a range sensor, and then using this representation for planning [1]. However, the memory complexity of these methods scales poorly with the size of the environment, and they do not exploit semantic information nor visual cues [2].

As an alternative, learning-based approaches also dubbed *experiential learning* [3] have gained momentum due to their ability to work directly with high-dimensional data (e.g., images) and reason about non-geometric concepts in a scene. Furthermore, these methods are more intuitive to use for non-expert users as they allow for goal positions to be specified using images of places or objects rather than coordinates in a metric space [4]. However, end-to-end experiential learning generally learns a global controller that maps images directly to actions, failing to reason about long-horizon goals. Furthermore, they are well-known for being data inefficient [5], [6].



(a) First trajectory

(b) Second trajectory

Fig. 1: Navigation paths produced by O4A (Robot, blue) and by human teleoperation (Expert, magenta) in a 4.65m x 9.10m laboratory. When prompted with a goal image (red star), the robot uses its current front and back RGB observations (orange) to navigate towards the goal by minimizing a neural potential function via gradient descent. The paths were captured using information from a ViCON system, which was not available to the agent.

To overcome the challenges of long-horizon navigation, *topological* memory representations [7] are used to divide the navigation problem into two parts. First, the memory representation is used to produce a globally coherent navigation plan, which is then followed waypoint-by-waypoint using a learned or classical local controller [8]. Approaches that incorporate both memory and learning-based components are referred to as *semi-parametric*, while approaches that rely solely on learning are known as *fully-parametric*.

While semi-parametric methods have proven to be effective for image-based navigation both indoors [9], [10], [4], [11] and outdoors [12], [13], they still encounter memory issues. This is a result of the topological memory typically being encoded as a graph whose nodes represent visited states and edges represent traversability. As the environment size increases, more nodes and edges are required in the graph, increasing the memory requirements.

In addition, spurious connections in the graph can impede navigation performance as they may represent non-feasible transitions in the physical world, leading to failure modes in the global planning stage. Although the literature offers partial solutions to these limitations by pruning the graph with hand-crafted heuristics [10], [12], these methods add complexity to the problem and generally require tuning for each environment.

To address these limitations, we propose **One-4-All** (O4A), an end-to-end fully-parametric method for imagegoal navigation. O4A is trained offline using non-expert

<sup>\*</sup>Equal contribution. Author ordering determined by competitive duck-calling, where the winner was selected by a blind jury on their ability to recreate various duck calls.

<sup>&</sup>lt;sup>1</sup>Sacha Morin, Miguel Saavedra-Ruiz and Liam Paull are with the Department of Computer Science and Operations Research, Université de Montréal, Montréal, QC, Canada, and with Mila - Quebec AI Institute, Montréal, QC, Canada. sacha.morin@mila.quebec

<sup>&</sup>lt;sup>a</sup>Project page https://montrealrobotics.ca/o4a/.

exploration sequences of RGB data and controls. We first rely on self-supervised learning to identify neighboring RGB observations. Armed with this notion of connectivity, we compute a graph to derive a manifold learning [14], [15] objective for our planning module, which we dub the geodesic regressor. The geodesic regressor will learn to predict shortest path lengths between pairs of RGB images and in that sense, encodes the geometry of the environment and acts as our memory module [16], [17], [18], [19]. While we do compute a temporary graph during training, we discard it for navigation, and found that it does not require the handcrafted graph pruning heuristics of existing semi-parametric methods. Intuitively, we trade a potentially high number of nodes and edges in a graph for a fixed number of learnable parameters, thus mitigating the memory limitations of semiparametric approaches. Inference is also improved: graph queries are replaced with efficient forward passes in a neural network.

For navigation, we draw inspiration from potential fields planning [20] and use the output of our geodesic regressor as an attractor in a potential function. This allows us to frame navigation as a minimization problem, with the global minimizer being the goal image. We show how this navigation approach enables the robot to perform long-horizon navigation and succeed even in geometrically complex environments.

To summarize, our main contributions are:

- An offline self-supervised training procedure using nonexpert exploration sequences of RGB data and controls, without any depth or pose measurements;
- A graph-free, end-to-end navigation pipeline that avoids tuning graph pruning heuristics;
- A potential fields-based planner that avoids local minima and reaches long-horizon goals, thanks to a geodesic attractor trained with a manifold learning objective;
- An interpretable system that recovers the geometry of the environment in its latent space, even in the absence of any pose information.

We show that O4A achieves state-of-the-art indoor navigation in 8 simulated environments. We further provide a real-world evaluation using the Jackal UGV platform.

### II. RELATED WORK

The problem of robot navigation has been extensively studied [1]. In recent years, there has been a growing trend towards image-based learning approaches or experiential learning [3]. These approaches have the advantage of being able to reason about the geometry of an environment, as well as the semantic aspects of traversability, such as tall grass in a field [2]. In contrast, classical approaches that rely purely on the geometry of the environment through metric representations struggle with such semantic aspects, leading to inefficient navigation plans [21].

Reinforcement Learning (RL) agents are a prominent example of experiential learning and have been widely employed for image-based embodied navigation [19], [22], [23]. While these approaches provide a sound solution to

the navigation problem, RL policies are known to be datahungry, with some *offline* RL methods requiring up to 30 hours of training data [6]. Moreover, one of the key challenges of RL is their limited navigation capabilities over long horizons [5].

To overcome the long horizon limitation, semi-parametric approaches use a topological memory encoded as a graph [7]. Examples in the literature [4], [8], [9], [10], [12], [24], [25], [26] use this topological memory as a *global planner* to obtain navigation waypoints that guide the agent towards a goal and a *local policy* to navigate between these waypoints. However, these methods have two significant limitations. First, spurious connections in the graph can adversely affect the planner's ability to derive a feasible plan (e.g., connections that allow warping between obstacles). Secondly, these methods do not scale well in terms of memory as the number of vertices and edges in the graph increases with the size of the environment.

These limitations are partially addressed by hand-crafted heuristics. Examples of these include connectivity thresholds to prune the number of spurious edges [9], [24], node sparsification strategies [8], [25] and lifelong updates to the graph [10]. However, these methods end up adding a nonnegligible number of parameters that require tuning and are often environment dependant. In contrast, we do not rely on such heuristics and use the raw connectivity derived from a connectivity classifier trained on top of a backbone, which is trained using contrastive learning (i.e., explicitly maintain neighboring RGB observations close in a latent space while also pushing away non-neighboring observations [15]).

Of particular interest to this work are Semi-Parametric Topological Memory (SPTM) [9] and Visual Navigation with Goals (ViNG) [12]. SPTM uses a classifier to determine the connectivity between two temporally close images and creates an unweighted graph based on this. This graph does not accurately reflect the distance between two close or distant samples as they are not weighted, exacerbating the spurious edges issue. Similarly, ViNG uses a classifier to estimate the temporal number of steps between samples and weight the edges of the graph with these estimates. Planning is performed over the graph and a relative pose predictor is paired with a PD controller to navigate waypoints. Both methods employ pruning and sparsification strategies. Our method does not prune the graph and directly estimates the action between two samples, allowing us to predict connectivity and local controls simultaneously.

Additionally, both SPTM and ViNG create a graph using *all* training images and produce navigation plans by querying the graph using Dijkstra's algorithm [27]. In contrast, we use our latent codes to weight a training graph and learn to predict shortest path lengths over it with a geodesic regressor, similar to Plan2Vec [15]. This allows to address the memory limitation of graph-based methods and enables the estimation of shortest path distances over both seen and unseen images in an environment.

There has also been research on alternative memory representations for embodied navigation, including the use of

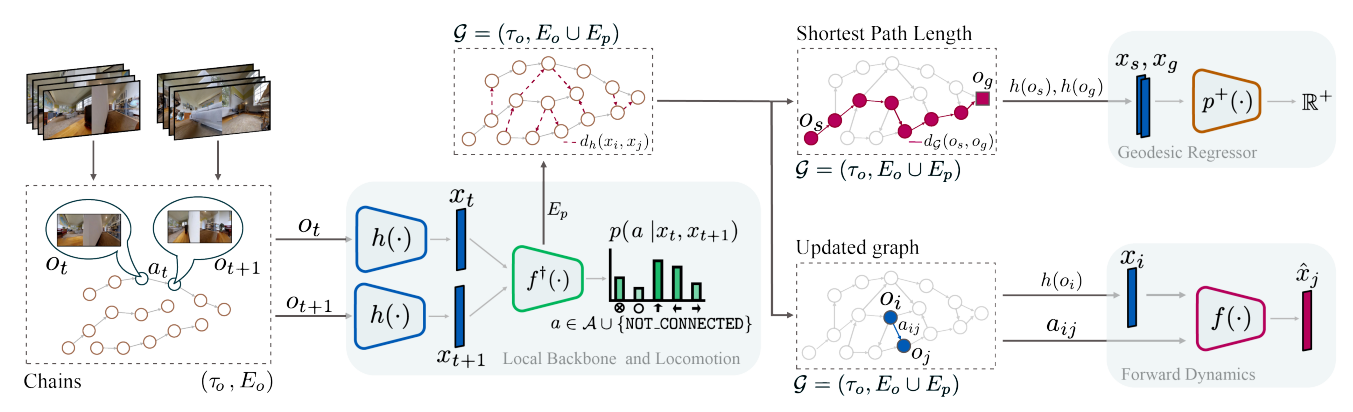


Fig. 2: O4A consists of 4 learnable modules for image-goal navigation. Learning is entirely achieved using previously collected RGB observation trajectories  $\tau_o = \{o_t\}_{t=1}^T$  and corresponding actions  $\tau_a = \{a_t\}_{t=1}^T$ , without pose. The **local backbone** h (left) takes as input RGB images to produce low-dimensional latent codes  $x \in \mathcal{X}$ . The **locomotion head**  $f^{\dagger}$  (center) uses pairs of latent codes to predict the action required to traverse from one latent code to the other (order matters), or the inability to do so through the NOT\_CONNECTED output. h and  $f^{\dagger}$  are then used to construct a directed graph  $\mathcal{G}$ , where nodes represent images and edges represent traversability. The **forward dynamics head** (bottom right) f is trained using edges from  $\mathcal{G}$  to predict the next code  $x_j$  given the current code  $x_i$  and an action  $a_{ij} \in \mathcal{A}$ . The geometry of the graph  $\mathcal{G}$  is embedded in a neural network using a **geodesic regressor**  $p^+$  (top right), which outputs the shortest path length for any pair of codes. Once all the modules are trained,  $\mathcal{G}$  can be discarded, and  $p^+$  be used as part of a potential function, as illustrated in Figure 3 and detailed in Equation 5.

semantic [11], [17], [28], spatial [16], [18], [29] or embedding representations [19]. To the best of our knowledge, none of these representations exploit a training graph to obtain a geodesic regressor for navigation. Our approach is inspired by Plan2Vec [15] which is a pure planning method and uses its geodesic regressor (referred to as global metric) as a heuristic for graph search. O4A instead tackles planning and navigation simultaneously and uses the geodesic regressor in a potential function to frame navigation as a simple minimization problem [20].

Finally, several existing methods rely on access to ground truth pose information in order to learn temporal estimates or relative pose between samples [8], [10], [12], [26]. Our method can be trained in a self-supervised manner using only raw RGB image samples and actions, making it independent of pose information.

### III. METHOD

## A. Problem Definition

We consider a robot with a discrete action space  $\mathcal{A} = \{ \text{STOP}, \text{FORWARD}, \text{ROTATE\_RIGHT}, \text{ROTATE\_LEFT} \}$  for an image-goal navigation task [30]. Using our knowledge of the robot's geometry and an appropriate exteroceptive onboard sensor (e.g., a front laser scanner), we assume that the set of collision-free actions  $\mathcal{A}_{free}$  can be estimated.

When prompted with a goal image  $o_g$ , the agent should navigate to the goal location in a partially observable setting using only RGB observations  $o_t$  and the  $\mathcal{A}_{free}$  estimates. The agent further needs to identify when the goal has been reached by *autonomously* calling the STOP action in the vicinity of the goal [30].

# B. Data

We aim to achieve image-goal navigation using learned modules parameterized by deep neural networks. For any given environment, we assume that some previously collected observation trajectory  $\tau_o = \{o_t\}_{t=1}^T$  and corresponding actions  $\tau_a = \{a_t\}_{t=1}^T$  are available. We consider a single trajectory from a single environment for notational conciseness, but in practice use multiple data trajectories (Fig. 2) from different environments. We do not require an expert data collection policy and the dataset could be the product of teleoperation, self-exploration or random walks, as long as it sufficiently covers the free space of the environment. Of note, we tackle navigation in an unsupervised setting and do not assume access to pose estimates for each image observation, which greatly simplifies data collection. Moreover, we do not collect any depth measurement, and only rely on a front laser scanner at runtime for simple collision checking.

# C. System

- a) Overview: We illustrate and present an overview of our system in Figure 2. We first rely on self-supervised learning to learn an RGB backbone paired with a connectivity head to infer a graph over all images in  $\tau_o$ . The graph will then be used to derive training objectives for a forward dynamics module and a geodesic regressor. We finally show how to navigate the trained system in Subsection III-D.
- b) Local Backbone: The local backbone learns a mapping from raw images to low-dimensional latent codes  $h: \mathcal{O}_{RGB} \to \mathcal{X}$ . For simplicity, we will denote extracted features as x = h(o). The function h will serve a dual purpose: 1) to extract low-dimensional features in  $\mathcal{X} = \mathbb{R}^n$  that will be used as input for other modules, and 2) to learn a **local metric** defined as

$$d_h(x_t, x_s) = ||x_t - x_s||_2 \tag{1}$$

between pairs of observations. Given the lack of pose information in the training data, h is trained via self-supervised learning using the siamese loss [15]

$$\mathcal{L}_{h}(x_{t}, x_{t+1}, \mathcal{N}) = (m_{+} - d_{h}(x_{t}, x_{t+1}))^{2} + \frac{1}{|\mathcal{N}|} \sum_{x^{-} \in \mathcal{N}} \max(0, m_{-} - d_{h}(x_{t}, x^{-}))^{2},$$
(2)

where  $m_+$ ,  $m_- \in \mathbb{R}^+$ ,  $m_+ < m_-$  are positive and negative margins, respectively, and  $\mathcal{N}$  is a set of random data from  $\tau_o$ , which are used as so-called negatives. Equation 2 is an instance of time contrastive learning: consecutive observations (positive pairs), which we know to be indeed close in terms of pose, are encouraged to be at a distance of exactly  $m_+$  in  $\mathcal{X}$ . Negatives are pushed to be at least at a distance of  $m_-$ , reflecting the fact they should not share the same neighborhood even if the exact distance between them is unknown at this stage. This latest observation motivates the term "local metric" [15], since the actual distance  $d_h$  is only informative when applied to positive pairs that are close in latent space. It should be stressed that  $d_h$  cannot predict how far negative pairs are apart in general, as it tends to saturate around  $m_-$  as discussed in [15].

c) Locomotion Head: The component  $f^{\dagger}: \mathcal{X} \times \mathcal{X} \to \mathcal{A} \cup \{\text{NOT\_CONNECTED}\}$  predicts the action needed to travel between two latent codes, or returns the NOT\_CONNECTED token when the transition is deemed not feasible in a single action.  $f^{\dagger}$  therefore acts as both a loop closing module and an inverse dynamics predictor. It is trained using the standard cross-entropy loss on the actions observed in  $\tau_a$ . We use the same negatives  $\mathcal{N}$  from Equation 2 to train the NOT\_CONNECTED class.

Even if most negatives in  $\mathcal{N}$  are true negatives (in the sense that the observations are not connectable with one action step), both h and  $f^{\dagger}$  can be exposed to occasional false negatives during training (e.g., if the same location is visited twice, the induced observations won't be temporally consecutive and can appear in  $\mathcal{N}$ ). These false negatives in fact correspond to the loop closures that should be discovered by the trained system in the data. Perhaps surprisingly, it turns out that  $f^{\dagger}$  makes "fortuitous mistakes" and does predict a number of loop closures properly, therefore overcoming to some degree the imperfections in its training objective. This property allows self-supervised methods to learn useful data representations in the absence of a clean supervisory signal (for navigation, the relative pose between images).

d) Graph Construction: Equipped with h and  $f^{\dagger}$ , we can now build a **directed graph**  $\mathcal G$  whose edges are weighted using  $d_h$  (Equation 1). We first treat the collected data as a chain graph with observed edges  $E_o = \{(o_t, o_{t+1}) : o_t, o_{t+1} \in \tau_o\}$  and then run pairwise computations to obtain new loop closure edges  $E_p = \{(o_t, o_s) : o_t, o_s \in \tau_o, f^{\dagger}(x_t, x_s) \in \mathcal{A}\}$ . The final graph is denoted by  $\mathcal{G} = \{(o_t, o_s) : o_t, o_s \in \tau_o, f^{\dagger}(x_t, x_s) \in \mathcal{A}\}$ .

 $(\tau_o, E_o \cup E_p)$ . No additional post-processing of the graph is required, contrary to existing methods [9], [10], [12], [25] which can require tuning numerous hyperparameters to curate nodes and edges.

e) Forward Dynamics Head: The forward dynamics head is denoted by  $f: \mathcal{X} \times \mathcal{A} \to \mathcal{X}$  and trained using edges/transitions from  $\mathcal{G}$ . For any edge  $(o_t, o_s)$  in  $\mathcal{G}$  during training, the module is trained with the mean squared error loss to approximate the function  $(x_t, f^{\dagger}(x_t, x_s)) \mapsto x_s$ , using the locomotion head  $f^{\dagger}$  to provide an input action even if none was observed. f will therefore benefit from additional transitions in  $E_p$  that were not initially observed in  $E_o$ . The above is an instance of semi-supervised learning called cotraining [31], in which the functions h and  $f^{\dagger}$  are used to label unseen transitions in the training set, thus enhancing the supervisory signal that is employed to train f.

f) Geodesic Regressor: The final component and core navigation module  $p^+: \mathcal{X} \times \mathcal{X} \to \mathbb{R}^+$  learns to predict the shortest path lengths on  $\mathcal{G}$ . We denote these distances as  $d_{\mathcal{G}}(o_t,o_g)$  and compute them with Dijkstra's algorithm.  $d_G$  is defined over observation pairs from the discrete vertex set of  $\mathcal{G}$ . We aim to extend it over the continuous latent space  $\mathcal{X}$  to predict shortest path lengths for any pair of images at runtime. The training loss of the geodesic regressor is

$$\mathcal{L}_{p^{+}}(o_{s}, o_{t}) = (p^{+}(x_{s}, x_{t}) - d_{\mathcal{G}}(o_{s}, o_{t}))^{2}.$$
(3)

Interpreting observations as samples from a manifold embedded in the high-dimensional RGB space, the backbone h learns an embedding with locally Euclidean neighborhoods  $(d_h)$ , which are chained together by the graph search to compute the geodesic (intrinsic) distance over the entire manifold. Equation 3 in fact corresponds to a manifold learning objective [15], [14], and we will show the O4A training results in interpretable visualizations of the environment in Figure 4.

Once all the components have been trained,  $\mathcal{G}$  can be discarded and is not required for deploying the system. Indeed, both f and  $p^+$  will provide all the required information for image-goal navigation, as we will detail in Subsection III-D. In fact, the geodesic regressor  $p^+$  can be interpreted as encoding the geometry of  $\mathcal{G}$ , thereby trading a potentially high number of nodes and edges for a fixed number of learnable parameters.

g) Multiple Environment Setting: When k environments are considered, we train both h and  $f^{\dagger}$  on the entire data. To provide a more challenging task for the model, we sample negatives  $\mathcal N$  from either the same environment or a different one. h and  $f^{\dagger}$  can then be used to close loops and compute a set of graphs  $\{\mathcal G_i\}_{i=1}^k$ , one per environment. The forward dynamics f are then trained using transitions from all the graphs. Finally, each  $\mathcal G_i$  is used to train a geodesic regressor  $p_i^+$ . In summary, h,  $f^{\dagger}$  and f are shared across environments while  $p_i^+$  is environment-specific.

# D. Navigation

In this section, we discuss how to deploy O4A for navigation. Our approach is strongly inspired by Artificial Potential

Field (APF) methods [20], which plan motions over the agent configuration space by defining A) an attractive potential around the goal, and B) repulsive potentials around obstacles, allowing the agent to minimize the total potential function via gradient descent to reach the goal while avoiding obstacles.

As with APF, O4A will navigate by minimizing an attractor located at at the goal. Since actual agent and goal states are unobserved, the potential computations occur over the latent space  $\mathcal{X}$ , i.e. the extracted latent features of the agent and goal RGB observations. As the attractor, we use the geodesic regressor  $p^+$  which estimates the geodesic distance to the goal. Critically, this attractor factors in the environment geometry and can, for example, drive an agent out of a dead end to reach a goal that is close in terms of Euclidean distance, but far geodesically (c.f. Fig. 3). This property is somewhat reminiscent of navigation functions in APF literature [20], a special class of potential functions with a unique global minimizer at the goal, among other properties.

# Algorithm 1 Navigation

**Input**: env, goal image  $o_g \in \mathcal{O}_{RGB}$ , thresh  $\in \mathbb{R}^+$ , backbone h, forward dynamics f, collision detection function  $\gamma$ , potential function  $\mathcal{P}$ 

```
o, scan \leftarrow env.initialize()
                                                                     ▶ RGB and scan
x \leftarrow h(o)
x_g \leftarrow h(o_g)
\mathcal{B} \leftarrow \{x\}
while d_h(x, x_a) > thresh do
     \mathcal{A}_{free} \leftarrow \gamma(\mathtt{scan})
     a^* \leftarrow \underset{a \in \mathcal{A}_{free}}{\operatorname{arg\,min}} \ \mathcal{P}(f(x, a), x_g, \mathcal{B})
                                                                                    ⊳ Eq. 5
      o, scan \leftarrow env.step(a^*)
                                                                     ▶ RGB and scan
      x \leftarrow h(o)
      \mathcal{B} \leftarrow \mathcal{B} \cup \{x\}

    □ Update visited states

end while
env.step(STOP)
```

In practice, we found that minimizing  $p^+$  alone did not suffice to successfully navigate. The agent would often end up thrashing between two poses due to a local minimum in the attractor landscape, which can occur due to learning errors and the discrete action space. We therefore found it useful to define a latent repulsor function, which is only active in a certain radius  $m_r \in \mathbb{R}^+$ :

$$p^{-}(x_t, x_s) = \max(0, m_r - d_h(x_t, x_s)). \tag{4}$$

We use  $p^-$  to drive the agent away from previously visited states, the representations of which are saved in a buffer  $\mathcal{B}$ . By combining repulsors around observations in  $\mathcal{B}$  and the geodesic attractor  $p^+$ , we obtain a total potential function of

$$\mathcal{P}(x_t, x_g, \mathcal{B}) = p^+(x_t, x_g) + \sum_{x \in \mathcal{B}} p^-(x_t, x)$$
 (5)

where  $x_t$  and  $x_g$  represent the encodings of the current and

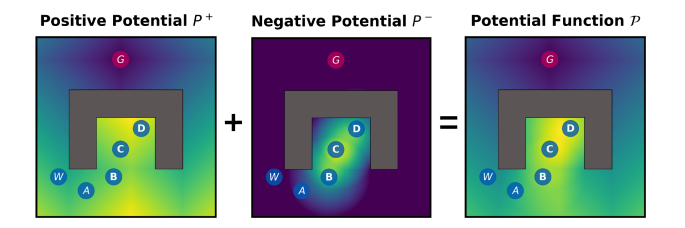


Fig. 3: An illustration of our potential function  $\mathcal{P}$  (Equation 5). Darker colors indicate lower potential. (Left) Geodesic attractor, which reflects the geodesic distance to the goal G. (Center) Visited state repulsors (B, C, D). (Right) Total potential function  $\mathcal{P}$ , which can be minimized by the agent at A by picking an appropriate waypoint W.

goal RGB images, respectively.

The detailed navigation procedure is presented in Algorithm 1. During navigation, our agent greedily minimizes  $\mathcal{P}$  by finding the best candidate action using forward dynamics over the set  $\mathcal{A}_{free}$  estimated by a collision detection function  $\gamma$ . This stands in contrast to APFs, since we blacklist collision-inducing actions instead of explicitly modeling repulsors around obstacles. In practice, since the agent rotates in place, we suppose that only the FORWARD action can cause collisions, which greatly simplifies the collision detection  $\gamma$ : we simply define a scan collision box in front of the robot based on its geometry.

It should also be noted that the STOP action is never included in  $\mathcal{A}_{free}$ , instead we found that thresholding the local metric  $d_h$  was a more reliable way of calling STOP in the vicinity of the goal.

### IV. EXPERIMENTS

We assess our approach in both simulated and real-world environments. The agent is a differential drive robot with two RGB cameras, one facing forward and the other facing backward, each with a field of view of  $90^{\circ}$ . Each image has a resolution of  $96\times96$  pixels. Consistent with [32], the robot moves FORWARD by 0.25m and ROTATE by  $15^{\circ}$ .

### A. Implementation details

All our models are trained using a batch size of 512. The local backbone uses a ResNet 18 encoder [34], followed by 5 1D convolutions to fuse the latent codes of the front and rear facing cameras. The locomotion head is composed of 4 linear layers. Both the local backbone and locomotion heads are jointly trained for 410,000 gradient steps, using  $m_{+}=1$  and  $m_{-}=10$ . The forward dynamics model has 4 linear layers and is trained for 330,000 steps. The geodesic regressor has 6 linear layers, and the same architecture is used for all environments, with training also carried out for 330,000 steps for each regressor. All models are trained using image augmentations and linear layers are followed by ReLU non-linearities. The models are trained using the Adam optimizer [35] with learning rate  $5e^{-4}$ . Navigation is performed with  $|\mathcal{B}| = 500$ ,  $m_r = 2.5$  and thresh = 3.5 throughout environments and experiments.

TABLE I: Average navigation performance over 8 simulated Gibson environments for One-4-all (O4A) and relevant baselines. We further study two additional variants of O4A by ablating terms in the potential function (Equation 5). We also denote which methods rely on a graph (G) for navigation and oracle stopping (other methods need to call STOP autonomously). We find that O4A substantially outperforms baselines, achieving a higher Success Rate (SR), Soft Success Rate (SSR), Success Weighted by Path Length (SPL), and a competitive ratio of Collision-Free Trajectories (CFT).

	$\mathcal{G}$	Oracle Stop	Easy (1.5 - 3m)			Medium (3 - 5m)			Hard (5 - 10m)			Very-Hard (>10m)			
			SR↑	SSR↑	SPL↑	SR↑	SSR↑	SPL↑	SR↑	SSR↑	SPL↑	SR↑	SSR↑	SPL↑	CFT↑
Random	_	✓	0.49	0.49	0.32	0.24	0.24	0.15	0.07	0.07	0.04	0.01	0.01	0.01	0.94
GC-BC [33]	_	$\checkmark$	0.42	0.42	0.25	0.21	0.21	0.10	0.07	0.07	0.03	0.02	0.02	0.01	0.94
SPTM [9]	$\checkmark$	_	0.32	0.51	0.14	0.17	0.28	0.06	0.07	0.12	0.03	0.02	0.03	0.01	0.96
ViNG [12]	$\checkmark$	_	0.29	0.64	0.10	0.19	0.46	0.07	0.11	0.28	0.05	0.06	0.12	0.02	0.99
O4A (Ours)	_	_	0.95	0.97	0.65	0.93	0.95	0.65	0.90	0.92	0.65	0.85	0.88	0.65	0.96
O4A w/o p <sup>-</sup>	_	_	0.11	0.36	0.11	0.07	0.22	0.07	0.03	0.09	0.03	0.01	0.02	0.01	0.99
O4A w/o $p^+$	-	_	0.45	0.70	0.13	0.27	0.47	0.09	0.13	0.23	0.04	0.04	0.07	0.02	0.90

# B. Simulation

- a) Simulator & Data: We perform our experiments using the Habitat simulator [36] with the Gibson dataset [37]. We use the Gibson split defined in [36] and use eight environments from it: Hambleton  $(67m^2)$ , Annawan  $(75m^2)$ , Nicut  $(90m^2)$ , Dunmor  $(90m^2)$ , Cantwell  $(107m^2)$ , Sodaville  $(114m^2)$ , Aloha  $(114m^2)$  and Eastville  $(121m^2)$ . A total of 240,000 data points are collected by navigating random waypoints (resulting in very suboptimal trajectories) and split into a training set (70%) and a validation set (30%).
- b) Baselines: To assess the navigation performance of our method, we compare against the following baselines:
  - Random Agent. An agent sampling actions uniformly from A \ {STOP}, subject to collision checking. The policy relies on ground truth pose for oracle stopping.
  - Goal Conditioned Behavioral Cloning (GC-BC), adapted from [33]. We extended the method with Hind-sight Experience Replay (HER) [38] to relabel new goals and enhance the training signal for the agent. This policy also relies on ground truth pose to call STOP. We collected a distinct set of expert trajectories for this baseline.
  - SPTM [9]. This method is extended with hard-negative mining as proposed by [12] to improve generalization performance. To call STOP, we tune a threshold on the reachability estimator between current and goal images.
  - ViNG [12]. The PD controller of the original work is replaced by an oracle Habitat controller to handle discrete actions. We tune a threshold on the timestep predictor to call STOP.
  - O4A Without Latent Repulsors. The repulsors  $p^-$  are not used during navigation and the agent is driven towards the goal by greedily minimizing  $p^+$ .
  - **O4A Without Geodesic Regressor**. We discard the attractor  $p^+$  and only use the latent repulsors  $p^-$ .

To ensure a fair comparison, all the baselines have the same capacity and collision checking strategy as O4A. We substitute the neural architectures used in the baselines with our local backbone h and locomotion head  $f^{\dagger}$ . Baselines are trained for 415,000 gradient steps and tested with various hyperparameters, the best of which were used for benchmarking.

c) Evaluation: To assess the navigation performance, we rank the difficulty of each trajectory as proposed by [4]. Trajectories are categorized into easy  $(1.5-3\mathrm{m})$ , medium  $(3-5\mathrm{m})$ , and hard  $(5-10\mathrm{m})$  based on their geodesic distance to the goal. We add an extra category labeled as "very hard"  $(>10\mathrm{m})$  to evaluate the agent's ability to plan for long-horizon goals. Each difficulty level is assessed over 1,000 trajectories using a maximum episode length of 500. To ensure a comprehensive assessment, we sample distinct starting positions and goals for each environment and difficulty, resulting in a total of 4,000 trajectories per environment.

We assess navigation performance by measuring Success Rate (SR) and Success weighted by Path-Length (SPL) [30]. A navigation trial is considered successful if the agent comes to a STOP within a maximum distance of 1m from the goal. We also use a *Soft* Success Rate (SSR), where a trial is successful if the agent is less than 1m away from the goal at any point during navigation. Lastly, we monitor the ratio of Collision-Free Trajectories (CFT) across all difficulties. A trajectory is deemed collision-free if it does not collide during the experiment.

d) Results: We present quantitative navigation results in Table I. O4A successfully navigates to goals of all difficulty levels and outperforms all considered baselines. The tight gap between SR and SSR showcases the reliability of the STOP mechanism based on the local metric  $d_h$ . Surprisingly, the O4A SPL is stable across all difficulties, despite a decreasing success rate. This indicates that the quality of successful paths is in fact slightly better for distant goals. This observation, combined with visual evaluation of episodes, suggests that the O4A attractor provides a clearer signal for distant goals and is noisier when navigating nearby locations. The two O4A ablations confirm that all considered potentials in our potential function  $\mathcal P$  are essential contributors to success.

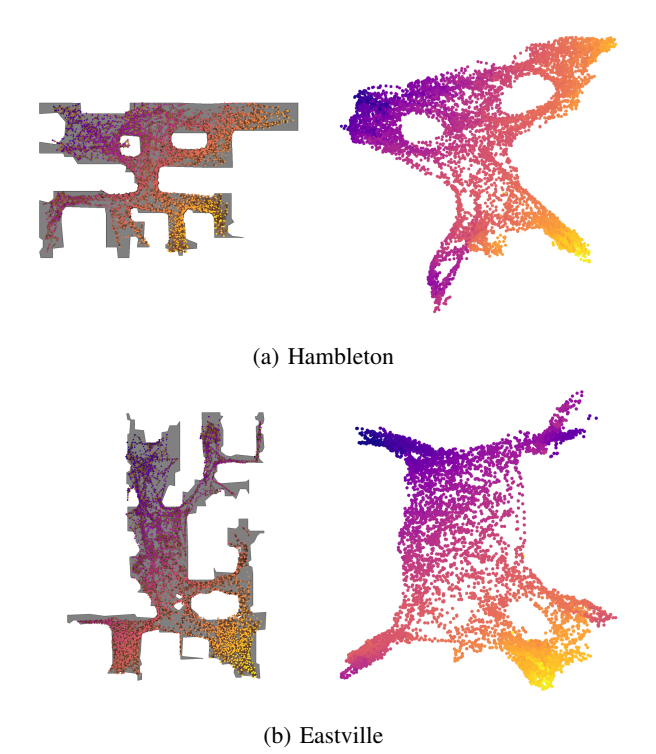


Fig. 4: (Left column) O4A graph connectivity over 2 Gibson environments. Points correspond to the location of RGB observations and are colored by the sum of their x and y coordinates. The graphs are free of egregious spurious edges, which allows to train effective geodesic regressors before discarding them. (Right column) 2 principal components of the last layer in the geodesic regressor  $p^+$  with the same coloring scheme. The unsupervised latent geometry is consistent with the environment geometry, and some topological features (e.g., the obstacle "holes") are evident in the latent space, even if the training of O4A never used pose information.

While the SPTM and ViNG performance are below those reported in the original papers, they are in line with recent comparable benchmarks in the literature [10]. The gap can be partially explained by variations in the experimental design. Neither method considers collisions nor how to stop when the goal is reached. Having STOP in the action space increases the challenge, due to the agent's ability to prematurely terminate episodes because of a false positive. We also note that SPTM considered omnidirectional actions, and that the original ViNG results focused on larger-scale problems in relatively open outdoor settings. The GC-BC results demonstrate how learning long-range navigation remains challenging for end-to-end methods.

On a more qualitative note, we further explore the O4A graph connectivity used for training, and show how it learns an interpretable latent space in Figure 4.

# C. Real-World Results

a) Robot Evaluation: For the real-world experiments we run O4A on the Jackal platform described in Figure 5. The experiments are conducted in a 4.65m x 9.1m laboratory.



Fig. 5: We use the Jackal UGV mobile platform using the RGB channels (no depth) of two Realsense D435i cameras with a  $90^{\circ}$  FOV. We detect forward collisions using a forward-facing Hokuyo laser scanner. We run O4A onboard using an Intel i7-8700 CPU with 32 GB of RAM. We did not require a GPU for navigation.

We collected a total of 21,000 RGB image samples via teleoperation and split them as in our simulation experiments.

For evaluation, we chose 9 interesting episodes (3 starting positions with 3 goal images each) and repeated each 3 times, for a total of 27 runs. The maximum episode length was set to 300 steps, although the robot ended up exceeding 150 steps on only 2 occasions. In addition to SR and SSR (Subsection IV-B), we evaluate the final distance to goal (DTG), the number of FORWARD steps, and the number of ROTATION steps. For context, we also teleoperated the robot over the same episodes to provide an estimate of human performance. All the models used for the real-world experiments are finetuned for 30,000 gradient steps starting from the best checkpoint obtained in the simulation experiments. We run navigation with  $|\mathcal{B}| = 300$ ,  $m_r = 2.5$  and thresh = 5.

b) Results: The Jackal navigation results are presented in Table II. O4A solves most episodes and achieves an average DTG of under 1m, even if most goals were not visible from the starting location and located up to 9 meters away. The maximal measured DTG was 1.74m. Interestingly, the number of O4A calls to the FORWARD action is comparable to human performance, meaning the O4A paths over the plane are competitive. Moreover, the robot collided only one time over all episodes using our collision checking strategy. Two episodes are shown in Figure 1.

TABLE II: Average Jackal navigation performance for O4A and human teleoperation over 27 episodes. We report the Success Rate (SR), Soft Success Rate (SSR), final Distance to Goal (DTG), number of FORWARD steps and number of rotation steps (ROT.).

	SR ↑	SSR ↑	DTG ↓	FORWARD $\downarrow$	ROT.↓
O4A	0.74	0.78	0.83	23	53
Human	0.96	1.00	0.46	20	18

# V. CONCLUSION

We presented **One-4-All**, a deep-learning based approach for learning image-goal navigation tasks. While our final trained system is graph-free, we still require learning a geodesic regressor for each environment to encode the geometry (in the same way current approaches need to build an environment-specific graph). Generalizing geodesic regression across environments is a promising area of research, since it could allow to completely skip the graph building stage in new settings. Moreover, the strict reliance on RGB data of our approach greatly simplifies data collection, meaning it could be potentially scaled to large-scale datasets [39] combining both indoor and outdoor data.

### REFERENCES

- [1] S. Thrun, W. Burgard, and D. Fox, *Probabilistic Robotics (Intelligent Robotics and Autonomous Agents)*. The MIT Press, 2005.
- [2] D. Shah, B. Eysenbach, N. Rhinehart, and S. Levine, "Rapid Exploration for Open-World Navigation with Latent Goal Models," in 5th Annual Conference on Robot Learning, 2021.
- [3] S. Levine and D. Shah, "Learning robotic navigation from experience: principles, methods and recent results," *Philos. Trans. R. Soc. Lond. B Biol. Sci.*, vol. 378, no. 1869, p. 20210447, Jan. 2023.
- [4] D. S. Chaplot, R. Salakhutdinov, A. Gupta, and S. Gupta, "Neural topological slam for visual navigation," in *Proceedings of the IEEE/CVF Conference on Computer Vision and Pattern Recognition*, 2020, pp. 12875–12884.
- [5] G. Dulac-Arnold, N. Levine, D. J. Mankowitz, J. Li, C. Paduraru, S. Gowal, and T. Hester, "Challenges of real-world reinforcement learning: Definitions, benchmarks and analysis," *Mach. Learn.*, vol. 110, no. 9, p. 2419–2468, sep 2021.
- [6] D. Shah, A. Bhorkar, H. Leen, I. Kostrikov, N. Rhinehart, and S. Levine, "Offline reinforcement learning for visual navigation," in 6th Annual Conference on Robot Learning, 2022.
- [7] B. J. Kuipers and T. S. Levitt, "Navigation and mapping in large scale space," AI Magazine, vol. 9, no. 2, p. 25, Jun. 1988.
- [8] S. Bansal, V. Tolani, S. Gupta, J. Malik, and C. Tomlin, "Combining optimal control and learning for visual navigation in novel environments," in *Conference on Robot Learning*. PMLR, 2020, pp. 420–429.
- [9] N. Savinov, A. Dosovitskiy, and V. Koltun, "Semi-parametric topological memory for navigation," in *International Conference on Learning Representations*, 2018.
- [10] R. R. Wiyatno, A. Xu, and L. Paull, "Lifelong topological visual navigation," *IEEE Robotics and Automation Letters*, vol. 7, no. 4, pp. 9271–9278, 2022.
- [11] N. Kim, O. Kwon, H. Yoo, Y. Choi, J. Park, and S. Oh, "Topological semantic graph memory for image-goal navigation," in 6th Annual Conference on Robot Learning, 2022.
- [12] D. Shah, B. Eysenbach, G. Kahn, N. Rhinehart, and S. Levine, "Ving: Learning open-world navigation with visual goals," in 2021 IEEE International Conference on Robotics and Automation (ICRA). IEEE, 2021, pp. 13 215–13 222.
- [13] D. Shah and S. Levine, "ViKiNG: Vision-Based Kilometer-Scale Navigation with Geographic Hints," in *Proceedings of Robotics: Science and Systems*, 2022.
- [14] J. B. Tenenbaum, V. de Silva, and J. C. Langford, "A global geometric framework for nonlinear dimensionality reduction," *Science*, vol. 290, no. 5500, pp. 2319–2323, 2000.
- [15] G. Yang, A. Zhang, A. Morcos, J. Pineau, P. Abbeel, and R. Calandra, "Plan2vec: Unsupervised representation learning by latent plans," in *Learning for Dynamics and Control.* PMLR, 2020, pp. 935–946.
- [16] S. Gupta, J. Davidson, S. Levine, R. Sukthankar, and J. Malik, "Cognitive mapping and planning for visual navigation," in *Proceedings of the IEEE conference on computer vision and pattern recognition*, 2017, pp. 2616–2625.
- [17] G. Georgakis, B. Bucher, K. Schmeckpeper, S. Singh, and K. Daniilidis, "Learning to map for active semantic goal navigation," in *International Conference on Learning Representations*, 2022.
- [18] J. F. Henriques and A. Vedaldi, "Mapnet: An allocentric spatial memory for mapping environments," in 2018 IEEE/CVF Conference on Computer Vision and Pattern Recognition, 2018, pp. 8476–8484.

- [19] K. Fang, F.-F. Li, S. Savarese, and A. Toshev, "Scene memory transformer for embodied agents in long time horizon tasks," in CVPR, 2019.
- [20] H. Choset, K. M. Lynch, S. Hutchinson, G. A. Kantor, and W. Burgard, Principles of robot motion: theory, algorithms, and implementations. MIT press, 2005.
- [21] J. Wang, T. Zhang, N. Ma, Z. Li, H. Ma, F. Meng, and M. Q.-H. Meng, "A survey of learning-based robot motion planning," *IET Cyber-Systems and Robotics*, vol. 3, no. 4, pp. 302–314, 2021.
- [22] E. Wijmans, A. Kadian, A. S. Morcos, S. Lee, I. Essa, D. Parikh, M. Savva, and D. Batra, "Dd-ppo: Learning near-perfect pointgoal navigators from 2.5 billion frames," in *International Conference on Learning Representations*, 2019.
- [23] Z. Rao, Y. Wu, Z. Yang, W. Zhang, S. Lu, W. Lu, and Z. Zha, "Visual navigation with multiple goals based on deep reinforcement learning," *IEEE Transactions on Neural Networks and Learning Systems*, vol. PP, pp. 1–11, 03 2021.
- [24] B. Eysenbach, R. R. Salakhutdinov, and S. Levine, "Search on the replay buffer: Bridging planning and reinforcement learning," in Advances in Neural Information Processing Systems, vol. 32, 2019.
- [25] S. Emmons, A. Jain, M. Laskin, T. Kurutach, P. Abbeel, and D. Pathak, "Sparse graphical memory for robust planning," *Advances in Neural Information Processing Systems*, vol. 33, pp. 5251–5262, 2020.
- [26] X. Meng, N. Ratliff, Y. Xiang, and D. Fox, "Scaling local control to large-scale topological navigation," in *International Conference on Robotics and Automation (ICRA)*. IEEE, 2020, pp. 672–678.
- [27] E. W. Dijkstra, "A note on two problems in connexion with graphs," Numerische mathematik, vol. 1, no. 1, pp. 269–271, 1959.
- [28] S. K. Ramakrishnan, D. S. Chaplot, Z. Al-Halah, J. Malik, and K. Grauman, "Poni: Potential functions for objectgoal navigation with interaction-free learning," 2022 IEEE/CVF Conference on Computer Vision and Pattern Recognition (CVPR), pp. 18868–18878, 2022.
- [29] D. S. Chaplot, D. Gandhi, S. Gupta, A. Gupta, and R. Salakhutdinov, "Learning to explore using active neural slam," in *International Conference on Learning Representations (ICLR)*, 2020.
- [30] P. Anderson, A. Chang, D. S. Chaplot, A. Dosovitskiy, S. Gupta, V. Koltun, J. Kosecka, J. Malik, R. Mottaghi, M. Savva et al., "On evaluation of embodied navigation agents," arXiv preprint arXiv:1807.06757, 2018.
- [31] A. Blum and T. Mitchell, "Combining labeled and unlabeled data with co-training," in *Proceedings of the Eleventh Annual Conference on Computational Learning Theory*, ser. COLT' 98. New York, NY, USA: Association for Computing Machinery, 1998, p. 92–100.
- [32] M. Hahn, D. S. Chaplot, S. Tulsiani, M. Mukadam, J. M. Rehg, and A. Gupta, "No rl, no simulation: Learning to navigate without navigating," *Advances in Neural Information Processing Systems*, vol. 34, pp. 26661–26673, 2021.
- [33] F. Codevilla, M. Miiller, A. López, V. Koltun, and A. Dosovitskiy, "End-to-end driving via conditional imitation learning," in 2018 IEEE International Conference on Robotics and Automation (ICRA). IEEE Press, 2018, p. 1–9.
- [34] K. He, X. Zhang, S. Ren, and J. Sun, "Deep residual learning for image recognition," in *Proceedings of the IEEE conference on computer* vision and pattern recognition, 2016, pp. 770–778.
- [35] D. Kingma and J. Ba, "Adam: A method for stochastic optimization," International Conference on Learning Representations, 12 2014.
- [36] M. Savva, A. Kadian, O. Maksymets, Y. Zhao, E. Wijmans, B. Jain, J. Straub, J. Liu, V. Koltun, J. Malik, D. Parikh, and D. Batra, "Habitat: A Platform for Embodied AI Research," in *Proceedings of the IEEE International Conference on Computer Vision (ICCV)*, 2019.
- [37] F. Xia, A. R. Zamir, Z. He, A. Sax, J. Malik, and S. Savarese, "Gibson env: Real-world perception for embodied agents," in *Proceedings of* the IEEE conference on computer vision and pattern recognition, 2018, pp. 9068–9079.
- [38] M. Andrychowicz, F. Wolski, A. Ray, J. Schneider, R. Fong, P. Welinder, B. McGrew, J. Tobin, O. Pieter Abbeel, and W. Zaremba, "Hind-sight experience replay," *Advances in neural information processing systems*, vol. 30, 2017.
- [39] D. Shah, B. Osinski, B. Ichter, and S. Levine, "Robotic Navigation with Large Pre-Trained Models of Language, Vision, and Action," in CoRR, 2022.